

Tilted discs in six poorly studied cataclysmic variables

Stefan Y. Stefanov,^{1,2}★ Atanas K. Stefanov³

¹*Institute of Astronomy and National Astronomical Observatory, Bulgarian Academy of Sciences, 72 Tsarigradsko Shose Boulevard, 1784 Sofia, Bulgaria*

²*Department of Astronomy, Sofia University "St. Kliment Ohridski", 5 James Bourchier Boulevard, 1164 Sofia, Bulgaria*

³*Department of Physics and Astronomy, University College London, Gower Street, London WC1E 6BT, UK*

Accepted XXX. Received YYY; in original form ZZZ

ABSTRACT

In this work, we search for negative superhumps (nSHs) in poorly studied cataclysmic variables using TESS data. We find three eclipsing binaries with nSH signatures: HBHA 4204-09, Gaia DR3 5931071148325476992, and SDSS J090113.51+144704.6. The last one exhibits IW And-like behaviour in archival ZTF data, and appears to have shallow, grazing eclipses. In addition, we detect nSH signatures in two non-eclipsing systems: KQ Mon and Gaia DR3 4684361817175293440, by identifying the orbital period from the superorbital-dependent irradiation of the secondary. We discover nSH signatures in one more system, [PK2008] HalphaJ103959, by using an orbital period from another work. An improved mass ratio – nSH deficit relation $q(\varepsilon_-)$ is suggested by us, which agrees with independent measurements on nova-like variables. With this relation, we estimate the mass ratios of all systems in our sample, and determine the orbital inclinations for the three that are eclipsing. All systems with discovered nSHs in this work are excellent targets for follow-up spectroscopic studies.

Key words: stars: activity – binaries: close – novae, cataclysmic variables – stars: individual: HBHA 4204-09, Gaia DR3 4684361817175293440, KQ Mon, SDSS J090113.51+144704.6, Gaia DR3 5931071148325476992, [PK2008] HalphaJ103959

1 INTRODUCTION

Cataclysmic variables (CVs) are binary systems that consist of a white-dwarf (WD) primary and a Roche-lobe filling secondary. Matter from the secondary flows through the first Lagrangian point and accretes on to the primary. In the case of a non-magnetic or a very weakly magnetic primary, this mass transfer happens through an accretion disc (Hellier 2001). In systems with mass-transfer rates of $\dot{M} \approx 1 - 5 \times 10^{-9} M_{\odot} \text{yr}^{-1}$, thermal instabilities arise in the accretion disc and cause repeating quasi-periodic outbursts. These outbursts usually occur once about every few months, last several days, and can increase the system brightness with up to ~ 5 mag. CVs with recorded outbursts are termed dwarf novae (DNe), whereas CVs with no recorded outbursts are termed nova-likes (NLs). In NLs, most of the flux originates from the accretion disc, which is in a hot steady state and is much brighter than the two system components. The orbital periods of this type of variables can range from ~ 1 h to more than 10 h. Not many CVs, however, are observed in the period range of 2–3 h. This phenomenon is called the “period gap” and is explained by transitions in evolutionary stages of this type of variables (see Warner 1995 for an encyclopedic description of CVs).

NLs can change their brightness on time-scales from seconds to millennia. Some systems have drops in brightness of several magnitudes, which can last from months to years. This behaviour is most commonly observed in systems with orbital periods (P_{orb}) near the upper edge of the period gap. Such drops in brightness are cate-

gorised as a low state of type VY Scl (King & Cannizzo 1998) and can also be displayed by magnetic CVs. VY Scl low states are likely caused by the reduction or the complete cessation of mass transfer in the system, which significantly decreases the flux coming from the disc. They are believed to be associated with the magnetic activity of the secondary. Star spots emerging on the first Lagrangian point may suppress mass transfer in the system (Livio & Pringle 1994), and the radius of the secondary itself can be affected by magnetic activity (Howell 2004). Yet, the exact mechanism of mass-transfer cessation during VY Scl episodes remains unknown.

Apart from low states and other long-term trends in brightness, CVs display an abundance of photometric variability on shorter time-scales. Roche-lobe geometry requires that the secondary takes a characteristic teardrop-like shape. As it orbits the barycentre, it presents different projections of itself to the observer, which introduces a photometric variability of period $P_{\text{orb}}/2$. A similar effect can occur when the secondary is strongly irradiated by the accretion disc. In that case, the visibility of the irradiated side of the secondary is dependent on the orbital phase of the system, and a light-curve modulation of period P_{orb} takes place.

Some CVs exhibit variations in brightness that have periods slightly shorter or slightly longer than P_{orb} . These variations are called “superhumps” and are believed to be caused by a precessing accretion disc. Superhumps can be of either positive (pSH) or negative (nSH) type, depending on the sign of $P_{\text{SH}} - P_{\text{orb}}$. They are well-studied and commonly seen in SU UMa stars, a DN subclass (e.g. Kato et al. 2009, 2017); as well as in NLs (Bruch 2023). For NLs in particular, Bruch gave a sample of 46 systems, 13 have had

★ E-mail: sstefanov@nao-rozhen.org

pSHs, 16 have had nSHs and 17 have had superhumps of both types at some point in the past (but not necessarily at the same time).

Each superhump type is associated with processes of different nature. pSHs are believed to be caused by an apsidally precessing accretion disc. In this case, the 3:1 resonance induces tidal deformations, the heat from which causing periodic changes in disc brightness (Whitehurst 1988; Hirose & Osaki 1990; Lubow 1991). On the other hand, nSHs can be explained with a retrograde nodal precession of a tilted accretion disc. The tilt allows for the mass-transfer stream to go deeper in the gravitational well of the primary, and thus to release more energy upon impact. The point of impact on the disc is commonly referred to as the "bright spot". The sweeping of the bright spot across the disc faces introduces an additional photometric variability that has a period equal to the beating of P_{orb} and the disc precession period P_{prec} (Wood et al. 2009; Montgomery 2009a), i.e.

$$\frac{1}{P_{\text{nSH}}} = \frac{1}{P_{\text{orb}}} + \frac{1}{P_{\text{prec}}}. \quad (1)$$

Superhumps of both types can be used to estimate some physical properties of these systems. The nSH deficit ε_- is defined as

$$\varepsilon_- = \frac{P_{\text{nSH}} - P_{\text{orb}}}{P_{\text{orb}}} \quad (2)$$

and has been shown to correlate with the mass ratio of the system $q = M_1/M_2$ in several works (e.g. Wood et al. 2009; Montgomery 2009a). A detailed study of nSHs can be found in Kimura et al. (2020b); Kimura & Osaki (2021), where Kepler photometry of the NL system KIC 9406652 was analysed. The light curve of this particular object has identifiable P_{orb} , P_{nSH} signals as well as superorbital ones (i.e. P_{prec} signatures).

In this work, we present our results from a search for nSHs in poorly studied CVs that are similar to KIC 9406652. Section 2 presents our methods for searching and data reduction, and gives a list of objects with discovered nSH signatures. Section 3 contains a literature review and discussion of each system we found to have nSH behaviour. In Section 4, we attempt to estimate some physical parameters in said systems, and in Section 5, we summarise the findings of this work.

2 ANALYSIS

2.1 Data from TESS

The Transiting Exoplanet Survey Satellite (TESS; Ricker et al. 2015) mission is an all-sky survey in the red-infrared that continues to provide with long-term measurements of remarkable photometric precision. The TESS Science Processing Operations Center pipeline (SPOC; Jenkins et al. 2016) offers light curves from two different reduction techniques: Simple Aperture Photometry (SAP) and Pre-Search Data Conditioning Simple Aperture Photometry (PDCSAP). A comprehensive comparison between the two is given in Kinemuchi et al. (2012). PDCSAP tries to reduce effects of instrumental nature, but can sometimes introduce systematics in periodograms, and analysis should proceed with care. Bruch (2022) found in particular that the additional conditioning in PDCSAP may distort DNe light curves, and chose to use the simpler SAP technique in order to search for periodic variations in CVs. We use SAP light curves too in all analysis to follow.

2.2 Photometric features of tilted accretion discs

Negative superhumps are direct evidence for a titled accretion disc, but finding their signatures is only possible in systems of known

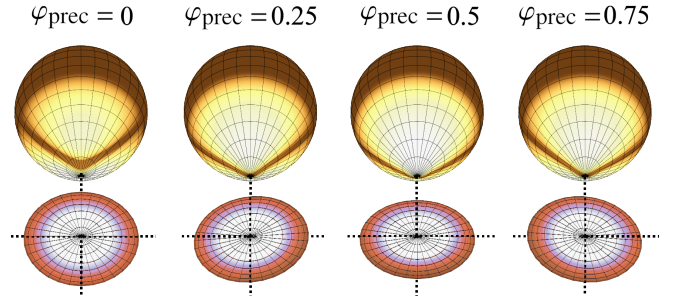


Figure 1. A model CV system at an orbital phase $\varphi_{\text{orb}} = 0.5$, as it would be seen by an observer. Four precession phases φ_{prec} of a disc with tilt $\theta = 6^\circ$ are illustrated. The orbital plane of the system is defined by dotted lines. It divides space into two half-spaces: the near (above the plane) and the far one (below the plane), with respect to the observer. The precession phase is defined such that the system is the brightest at $\varphi_{\text{prec}} = 0$. In this orientation, the disc has the largest projected area at $\varphi_{\text{prec}} = 0$. Conversely, at $\varphi_{\text{prec}} = 0.5$, it has the smallest projection, but faces towards the secondary and irradiates it the most. Kimura & Osaki (2021), Figure 9 gives a full description of CV configurations in titled-disc regimes.

P_{orb} . This is a strong restriction, since not many CVs have had their orbital periods measured. To expand the population of stars with known P_{orb} , we searched for systems with several significant peaks in the power spectrum, in a frequency region above the period gap. In the case of two neighbouring prominent peaks, it could be that those are signatures of P_{pSH} , P_{orb} and not P_{nSH} , P_{orb} . Nevertheless, this degeneracy can be lifted with the following rationale.

In systems with a precessing tilted accretion disc, the disc orientation changes with respect to the secondary for different orbital phases φ_{orb} and different disc precession phases φ_{prec} . The former is defined such that the secondary is at inferior conjunction at $\varphi_{\text{orb}} = 0.0$; the latter is defined¹ such that the light maximum in the disc precession cycle is at $\varphi_{\text{prec}} = 0.0$. The observed irradiation of the secondary by the bright disc varies with both φ_{prec} and φ_{orb} . Consider a non-eclipsing system at $\varphi_{\text{orb}} = 0.5$ (Figure 1). The orbital plane of the system divides space into two half-spaces, one of which the observer finds themselves in. One part of the system resides in the same half-space as the observer, and the other part is in the opposite half-space (i.e. on the other side of the orbital plane with respect to the observer). We shall refer to those as the "near half-space" and the "far half-space". As an example, in Figure 1, the part of the accretion disc that lies in the near half-space is: its rear side at $\varphi_{\text{prec}} = 0$, its right side at $\varphi_{\text{prec}} = 0.25$ and so on.

For an observer, the near half-space of a system is more photometrically accessible than the far half-space.² At $\varphi_{\text{prec}} = 0$, the luminous disc reveals the most of itself to the observer, and the average system brightness across φ_{orb} is the greatest. However, the irradiated region of the secondary is in the far half-space, and thus the φ_{orb} variation in brightness is minimal in amplitude. In the opposite case of $\varphi_{\text{prec}} = 0.5$, the observer sees the smallest possible projection of the disc, and the average system brightness across φ_{orb} is the smallest – but the irradiated region of the secondary is now in the near half-space, and the φ_{orb} variation in brightness is maximal in amplitude.

¹ These definitions are consistent with Kimura et al. (2020b).

² This is only untrue in the special case of $i = 90^\circ$, when the observer lies in the orbital plane, and both half-spaces are thus equally accessible.

At the same time, nSHs introduce additional complexities in variability that need to be accounted for. Kimura & Osaki (2021) discuss this issue and carry out the following procedure. A given light curve is initially split into subsets of different time intervals. Then, for each subset, they: (1) fold by P_{nSH} and construct an average light-curve profile of the nSH, (2) subtract said profile from each subset, (3) split the subset into different φ_{prec} windows, (4) fold each window by P_{orb} . This technique results in multiple orbital phase curves, each corresponding to a different φ_{prec} window. If these phase curves show a φ_{prec} -dependent irradiation of the secondary, the system has a precessing tilted accretion disc and the observed superhump is negative. It is this consideration that could lift the pSH-nSH degeneracy in the power spectrum.

In order to address the nSH contamination, we use a variant of the nSH-subtraction technique by Kimura & Osaki (2021) with the following adjustments: all data is smoothed by a fourth-order Savitzky-Golay filter (Savitzky & Golay 1964) of window size 10 d, and no separate subsets are considered; in (1), nSH light-curve profiles are constructed with median filters of window size 1101;³ in (3), four φ_{prec} intervals are considered with centres at $\varphi_{\text{prec}} = 0.00, 0.25, 0.50, 0.75$ and of width 0.1.⁴

2.3 Target selection

The International Variable Star Index (VSX; Watson et al. 2006, accessed 2022 June) is perhaps the most extensive catalogue of known variable stars. We took all objects from the VSX labelled as CV or as NL ($n = 1249$), and then sought all for which there were available TESS SPOC light curves of 120-second cadence ($n = 180$). Lomb-Scargle periodograms (LS periodogram; Lomb 1976; Scargle 1982) of range between $0.125 - 16.000 \text{ d}^{-1}$ were constructed for those systems. Periodograms were then manually searched for the simultaneous presence of at least two neighbouring periodicities in the region above the period gap, as well as for one periodicity near their expected beat period. This was done to select NLs with signatures of all $P_{\text{prec}}, P_{\text{orb}}, P_{\text{nSH}}$. For most stars, long-term photometry from the All-Sky Automated Survey for Supernovae (ASAS-SN; Shappee et al. 2014; Kochanek et al. 2017) and from the Catalina Sky Survey (CSS, Drake et al. 2009) was available. We attempted to construct LS periodograms using photometry from said surveys, but data was found to be sparse and of too long cadence to be usable.

We report on the discovery of nSH behaviour in six poorly studied CVs. Three of them are eclipsing systems, which enabled us to directly determine P_{orb} . For two other systems, P_{orb} was identified with the use of φ_{prec} -dependent irradiation of the secondary. The last CV was found to have P_{prec} and P_{nSH} signatures, but not a P_{orb} one. Our derived value of P_{orb} by Equation (1), however, agrees well with the spectroscopic measurement of Pretorius & Knigge (2008). All six objects are discussed individually in Section 3. During inspection, we also found five new eclipsing CVs with no superhump behaviour. Their measured orbital periods are provided in Table A3, and their orbital phase curves are shown in Figure A1.

3 REVIEW AND RESULTS

The following sections provide literature review, discussion and interpretation of data for all CVs with discovered nSH behaviour. Each

CV system has an associated figure containing: (1) available sky-survey data, (2) TESS photometry from sectors with prominent nSH behaviour together with corresponding LS periodograms, (3) orbital phase plots of data in the four φ_{prec} regions discussed in Section 2.2. Measured periodicities of each system are given in Table 1. All measurements agree well with Equation (1) within uncertainty.

3.1 HBHA 4204-09

HBHA 4204-09⁵ (Figure 2) is discovered by ASAS-SN. It was classified as a CV by Jayasinghe et al. (2018) and by ALeRCE (Förster et al. 2021) in data from the Zwicky Transient Facility (ZTF; Bellm et al. 2019). This object is part of the "Catalogue of Stars in the Northern Milky Way Having H-alpha in Emission" (Kohoutek & Wehmeyer 1999). The Gaia DR3 distance estimate is $478 \pm 3 \text{ pc}$ and ASAS-SN photometry gives a mean brightness of $m_V = 16.19 \text{ mag}$.

We report the presence of previously unknown V-shaped eclipses in HBHA 4204-09. Using them, we identify the periodogram peaks corresponding to $P_{\text{orb}}, P_{\text{nSH}}, P_{\text{prec}}$ (Table 1). Aside from these periodicities, the power spectrum contains a strong signal at $0^{\text{d}}070655(58)$, which matches $P_{\text{orb}}/2$. A collection of peaks at around $0^{\text{d}}155$ is observed, which may be indicative of a pSH signature. Additional photometry of HBHA 4204-09 can be found in TESS Sectors 55 and 56, but no superhumps are present in those data sources. Due to its high orbital inclination, the near and the far half-spaces defined by the orbital plane are comparably accessible to the observer. The portion of the secondary in the far half-space is most irradiated at $\varphi_{\text{prec}} = 0.00$, while the portion in the near half-space is most irradiated at $\varphi_{\text{prec}} = 0.50$. The orbital profiles in panels (d) and (f) of Figure 2 show stronger secondary irradiation at aforementioned φ_{prec} , which is expected.

3.2 Gaia DR3 4684361817175293440

Gaia DR3 4684361817175293440, hereinafter Gaia-468436⁶ (Figure 3) was discovered and classified as a NL type CV by Bajer (2019). The Gaia DR3 distance estimate is $1062^{+29}_{-30} \text{ pc}$. On the long-term ASAS-SN curve, a 1-mag fall in brightness can be observed around BTJD 800 – BTJD 1700. A panel with ASAS-SN photometry in this time period is shown in Figure 4. The observed drop in brightness has a smaller amplitude from what is expected in classic VY Scl low states. Quasi-cyclic variations of $P \sim 20 \text{ d}$ resembling Z Cam outbursts appear after the start of the low state. The system later returns to normal brightness and outbursts are replaced with a standstill lasting for ~ 300 days. This standstill is followed by another Z Cam outburst episode, after which no more outbursts of this type are observed.

Our LS periodogram of Gaia-468436 shows three peaks with periods matching Equation (1). We interpret them as $P_{\text{orb}}, P_{\text{nSH}}, P_{\text{prec}}$ in a system with a tilted precessing disc (Section 2.2). We find two additional peaks at $0^{\text{d}}07372(14)$ and $0^{\text{d}}07702(15)$ that match $P_{\text{nSH}}/2$ and $P_{\text{orb}}/2$ respectively. In Figure 3(d)–(g), it can be seen that the light maximum of orbital-phase curves gradually shifts to earlier φ_{orb} as the disc precession cycle advances. This is direct evidence for a retrogradely precessing tilted disc (Kimura et al. 2020b).

³ We found that this window size worked generally well for all systems.

⁴ That is, the intervals $0.95 - 0.05, 0.20 - 0.30, 0.45 - 0.55, 0.70 - 0.80$.

⁵ The VSX identifier of this source is ASASSN-V J210752.24+440542.0.

⁶ The VSX identifier of this source is BMAM-V424.

Table 1. List of CVs with discovered nSHs using the methods described in Section 2. All periodicities in this table were measured on a Lomb-Scargle periodogram of range 0.125–16 d⁻¹ and of ten-fold oversampling. All measured P_{prec} in this table agree within uncertainty with the expected values by Equation (1) using measured P_{orb} and P_{nSH} . Equatorial coordinates come from Gaia DR3 and are in the J2000 epoch.

Name	RA	Dec	TESS Sector	P_{orb}	P_{nSH}	P_{prec}	$ \varepsilon_- $
HBHA 4204-09	21 ^h 07 ^m 52 ^s .24	+44°05′42″.0	15, 16	0 ^d 14128(22)	0 ^d 13657(22)	4 ^d 11(18)	0.0333(22)
Gaia DR3 4684361817175293440	00 ^h 49 ^m 59 ^s .93	−76°08′27″.5	28	0 ^d 15401(53)	0 ^d 14750(52)	3 ^d 40(27)	0.0423(48)
KQ Mon	07 ^h 31 ^m 21 ^s .13	−10°21′49″.4	34	0 ^d 13456(40)	0 ^d 12894(38)	3 ^d 12(24)	0.0418(41)
SDSS J090113.51+144704.6	09 ^h 01 ^m 13 ^s .51	+14°47′04″.7	44–46	0 ^d 14631(17)	0 ^d 13991(17)	3 ^d 198(70)	0.0437(16)
Gaia DR3 5931071148325476992	16 ^h 36 ^m 03 ^s .63	−52°33′32″.6	39	0 ^d 14827(46)	0 ^d 14248(43)	3 ^d 57(30)	0.0391(42)
[PK2008] HalphaJ103959	10 ^h 39 ^m 59 ^s .98	−47°01′26″.3	36, 37	0 ^d 1577(2) [†]	0 ^d 15285(29)	4 ^d 94(26)	0.0308(22)

[†] Orbital period measured spectroscopically by Pretorius & Knigge (2008).

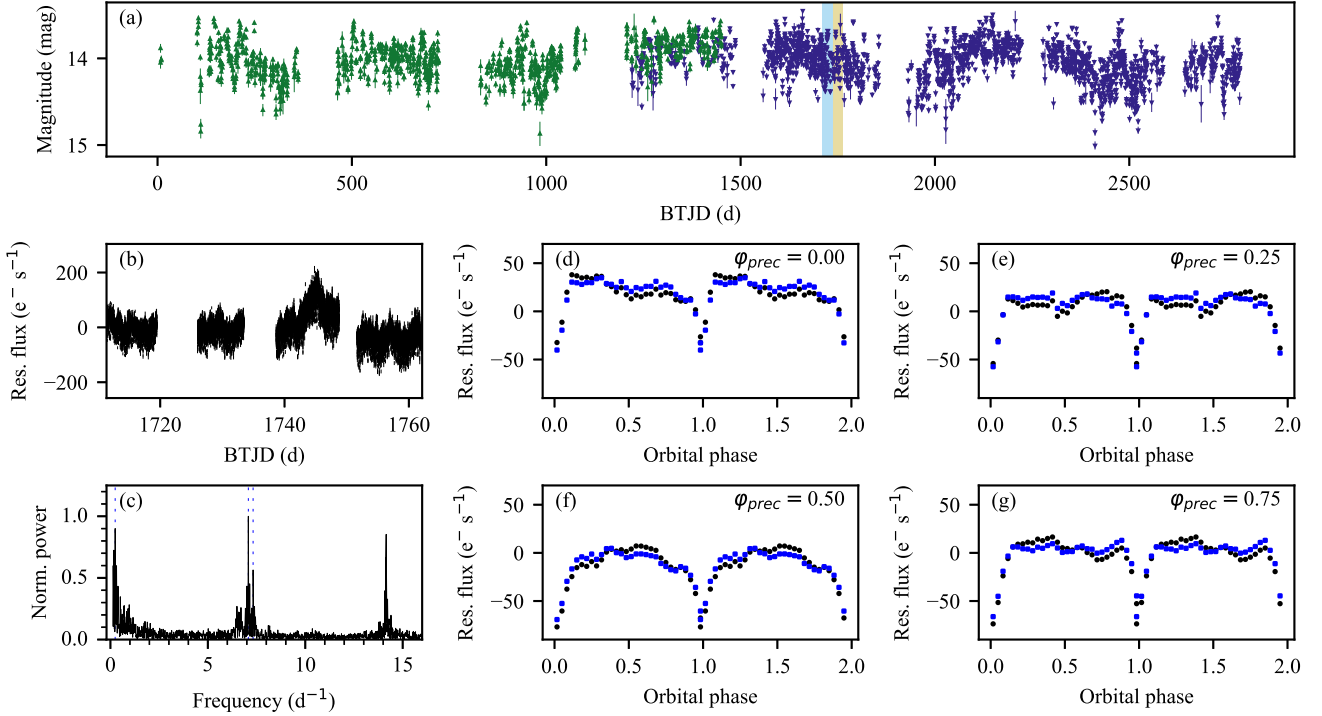


Figure 2. Photometry and analysis of HBHA 4204-09. (a) Long-term photometry from: ASAS-SN *g* (purple downward triangles), ASAS-SN *V* (green upward triangles). Temporal coverage of TESS: Sector 15 (light blue), Sector 16 (yellow). (b) Residual (mean-subtracted) SAP flux from TESS data. (c) Associated LS periodogram of (b), with indications of P_{prec} , P_{orb} , P_{nSH} signals from Table 1 (blue dashes). (d)–(g) Binned orbital profiles around disc precession phases $\varphi_{\text{prec}} = 0.00, 0.25, 0.50, 0.75$ with nSH subtraction (blue squares) and without one (black circles). The typical standard deviation of data in bins is 25 e⁻ s⁻¹. This system has a high inclination, and the parts of the secondary in both half-spaces are accessible to the observer. The secondary is expected to be the most irradiated in panels (d) and (f), where the observed out-of-eclipse profile is non-flat. In panels (e) and (g), where no irradiation of the secondary is expected, the out-of-eclipse profile is mostly flat.

3.3 KQ Mon

KQ Mon (Figure 5) was classified as a NL-type CV by Bond (1979) using low-resolution spectra in the optical. Its orbital period was measured in Schmidtbreick et al. (2005) to be $P_{\text{orb}} = 0^{\text{d}}1283(17)$ by analysing two nights of time-resolved spectroscopy. Later, Wolfe et al. (2013) examined far-ultraviolet spectra of KQ Mon from the International Ultraviolet Explorer. The mass of the primary was estimated to be $M_1 \sim 0.6 M_{\odot}$ with the use of synthetic spectra. The same work argued that the primary contributes little to the total system flux, and is overwhelmed by the flux of a steady-state accretion disc. It was concluded that the system is located at a distance of 144–159 pc, with an inclination of $i \leq 60^{\circ}$ and an accretion rate in the order of $\dot{M} \sim 10^{-9} M_{\odot} \text{ yr}^{-1}$. The Gaia DR3 distance is 628 ± 8 pc, which disagrees with their estimates.

Our measured value for P_{nSH} matches the P_{orb} given in Schmidtbreick et al. (2005). What we measure as $P_{\text{orb}} = 0^{\text{d}}13456(40)$ would have corresponded to a pSH signal in their interpretation. But then, no other signals in the periodogram would have been expected. We, however, measure a strong third signal at $3^{\text{d}}12(24)$, which is self-consistent with the other two by Equation (1). In addition, we observe a φ_{prec} -dependent amplitude of the orbital phase curve, which could be explained by a varying irradiation of the secondary. In Figure 3 of Schmidtbreick et al. (2005), a strong aliasing pattern can be seen. The authors chose an orbital period P_{orb} among four possible signals, two of which agree with our measurements of P_{orb} , P_{nSH} . With all this in mind, we think that the correct value of P_{orb} is $0^{\text{d}}13456(40)$, and that there is presence of a tilted accretion disc in this system.

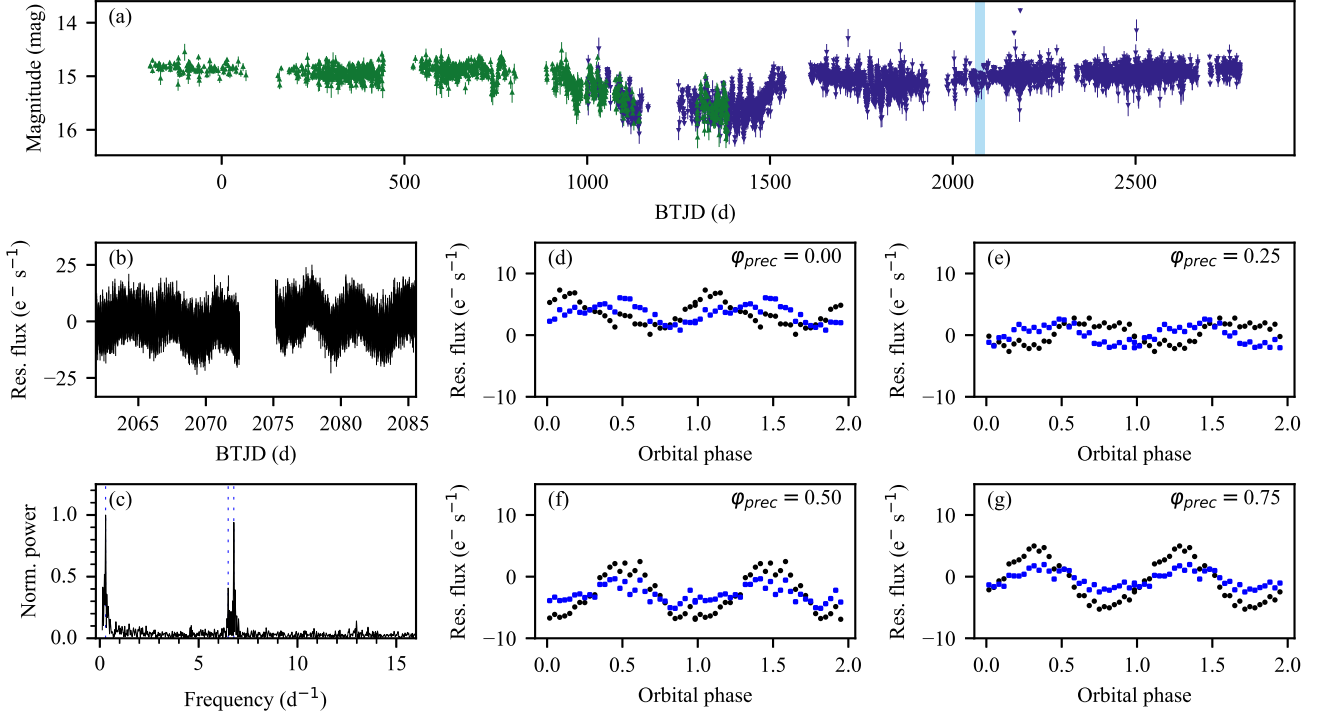


Figure 3. Photometry and analysis of Gaia-468436. (a) Long-term photometry from: ASAS-SN *g* (purple downward triangles), ASAS-SN *V* (green upward triangles). Temporal coverage of TESS: Sector 28 (light blue). (b) Residual (mean-subtracted) SAP flux from TESS data. (c) Associated LS periodogram of (b), with indications of P_{prec} , P_{orb} , P_{nSH} signals from Table 1 (blue dashes). (d)–(g) Binned orbital profiles around disc precession phases $\varphi_{\text{prec}} = 0.00, 0.25, 0.50, 0.75$ with nSH subtraction (blue squares) and without one (black circles). The typical standard deviation of data in bins is $4 \text{ e}^- \text{ s}^{-1}$. The effect of variable irradiation in panels (d)–(g) is similar to the one observed in KIC 9406652 (Kimura & Osaki 2021).

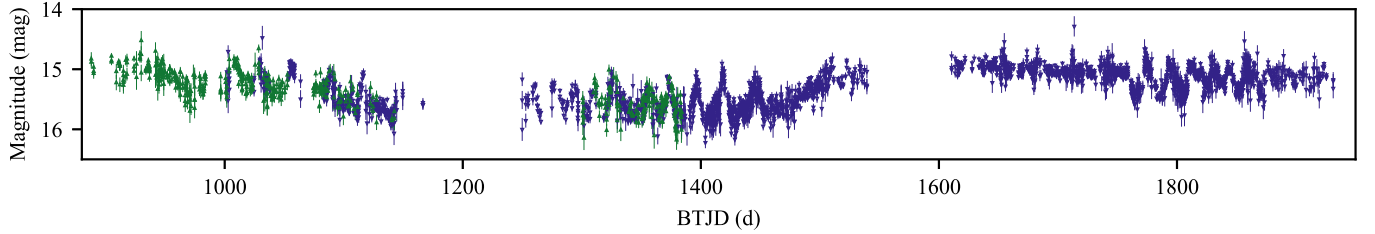


Figure 4. Z Cam-like episodes of Gaia-468436 in ASAS-SN *g* (blue downward triangles) and ASAS-SN *V* (green upward triangles). The Z Cam behaviour begins after a ~ 0.5 mag fall in brightness. Emerging oscillations have a variable amplitude of ~ 0.8 mag and are quasi-periodic with $P \sim 20$ days. At about BTJD 1500, a brightening takes place, which is followed by a standstill at a level of 15.0 mag. At about BTJD 1760, the standstill is replaced with another oscillatory episode that has outbursts of similar period and amplitude as the former ones. No more Z Cam episodes were observed in Gaia-468436 in this data.

3.4 SDSS J090113.51+144704.6

SDSS J090113.51+144704.6, hereinafter SDSS-090113 (Figure 6) first appeared in Szkody et al. (2009) where it was classified as a CV due to accretion disc features in its spectrum. This system was included in the catalogue of bright WDs of Raddi et al. (2017). Gaia DR3 estimated the distance to SDSS-090113 to be 1482^{+100}_{-116} pc. Later, Mösenlechner et al. (2022) included this system in their time-series analysis study of subdwarf A-type stars using Kepler K2 data. They discovered a periodicity of $0^{\text{d}}146$, which was suggested to be the orbital period P_{orb} .

SDSS-090113 has no recorded low states and its brightness varies around $m_V = 16.2$ mag. Between BTJD 1600 and BTJD 2300, we recognise an episode of anomalous Z Cam-type outbursts repeating

once about every 25 days (Figure 7). These outbursts begin after a brightening, which is one of the defining features of the IW And-phenomenon systems (Kato 2019). This can be explained by a tilted disc that causes the accretion stream to enter inner disc regions, and thus to disrupt the accretion cycle. In this new type of accretion, the inner disc is in a hot state, while the outer disc repeats outbursts (Kimura et al. 2020a).

Figure 6(d)–(g) shows what seems to be the presence of grazing eclipses in the orbital curve of SDSS-090113. They vary in depth and width, and for some phases of P_{prec} they disappear completely, similar to ES Dra (Kato 2022). Through them, we identify P_{orb} , P_{nSH} , P_{prec} (Table 1). Two additional peaks are found at $0^{\text{d}}071531(52)$ and $0^{\text{d}}073161(40)$ that match $P_{\text{nSH}}/2$ and $P_{\text{orb}}/2$ respectively.

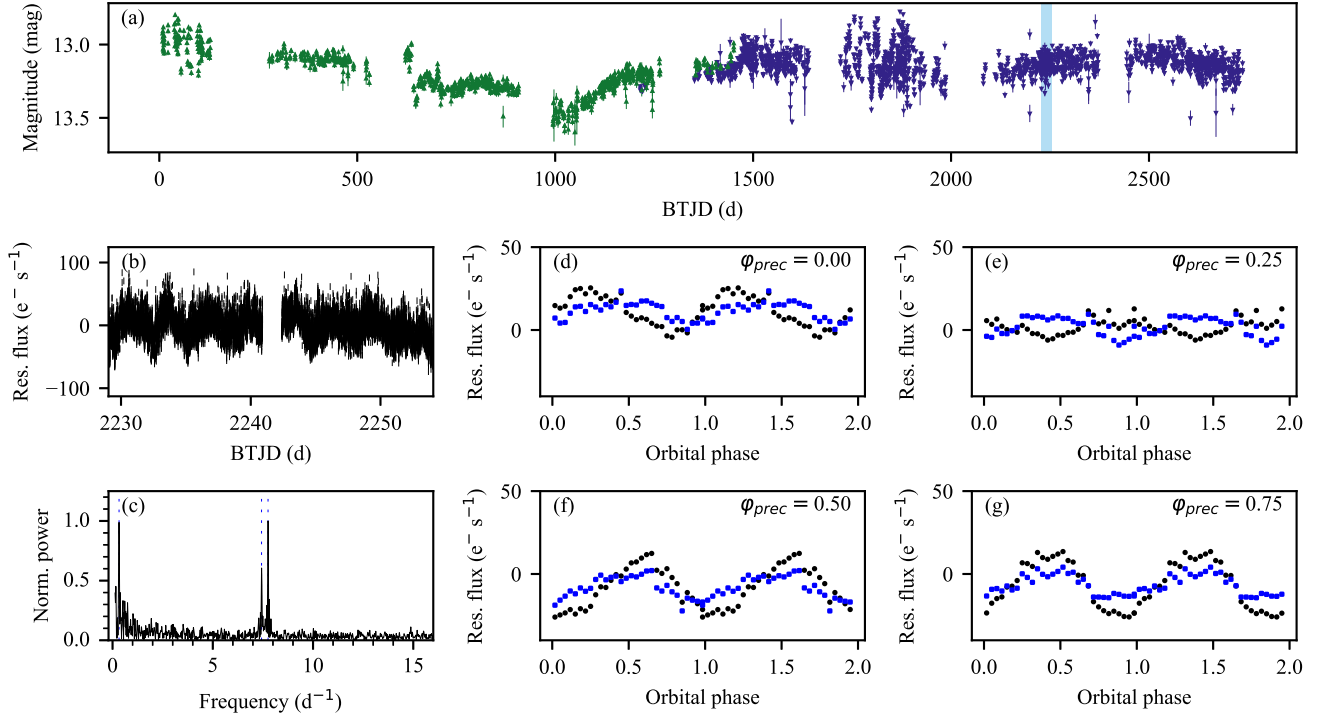


Figure 5. Photometry and analysis of KQ Mon. (a) Long-term photometry from: ASAS-SN *g* (purple downward triangles), ASAS-SN *V* (green upward triangles). Temporal coverage of TESS: Sector 34 (light blue). (b) Residual (mean-subtracted) SAP flux from TESS data. (c) Associated LS periodogram of (b), with indications of P_{prec} , P_{orb} , P_{nSH} signals from Table 1 (blue dashes). (d)–(g) Binned orbital profiles around disc precession phases $\varphi_{\text{prec}} = 0.00, 0.25, 0.50, 0.75$ with nSH subtraction (blue squares) and without one (black circles). The typical standard deviation of data in bins is $16 \text{ e}^- \text{ s}^{-1}$. The blue and the black curves differ due to the significant nSH contribution to the observed system flux. In blue curves of different φ_{prec} , there seems to be a change of shape and amplitude near $\varphi_{\text{orb}} = 0.5$, which is expected, but could be also due to noise. Kimura & Osaki (2021) provide models for such orbital curves that could explain these observations.

3.5 Gaia DR3 5931071148325476992

Gaia DR3 5931071148325476992, hereinafter Gaia-593107⁷ (Figure 8) is a poorly studied CV that was discovered in plates by Prestgard (2020) from the Digitized Sky Survey⁸ and the SuperCOSMOS *H α* survey (Parker et al. 2005). The NOMAD catalogue (Zacharias et al. 2004) gives an apparent magnitude of $m_V = 16$ mag. No ASAS-SN photometry is available for this system. Its TESS brightness reads $m_{\text{TESS}} = 16.02$ mag. There is an X-ray source (1RXS J163605.9-523335) at a distance of 20.8 arcsec, which is likely associated with Gaia-593107. In addition, we find two bright sources of brightness $m_{\text{TESS}} = 13.44$ and $m_{\text{TESS}} = 15.16$ mag in the aperture mask, that are expected to severely contaminate the light curve. This issue, however, is resolved by the apparent variability of Gaia-593107 in the discovery images⁹ of Prestgard, on the basis of which we attribute the tilted-disc behaviour to this specific system.

Our analysis of TESS light curves shows Gaia-593107 to be an eclipsing variable with an orbital period of $P_{\text{orb}} = 0^{\text{d}}.14248(43)$. A peak at $P_{\text{orb}}/2$ is present as well. This allows us to locate P_{orb} , P_{nSH} , P_{prec} (Table 1). A change in eclipse depth is observed in different phases of the determined φ_{prec} .

3.6 [PK2008] HalphaJ103959

[PK2008] HalphaJ103959, hereinafter PK-103959 (Figure 9) was classified as a CV in Pretorius & Knigge (2008), where spectroscopic and photometric analyses of the system were carried out. The orbital period of PK-103959 was measured to be $P_{\text{orb}} = 0^{\text{d}}.1577(2)$ in the same work. Catalina and ASAS-SN photometry has a mean brightness of $m_V = 15.7$ mag, with no low states. A gradual increase in brightness can be seen in the period between -1000 and 2000 BTJD.

We find signatures of P_{nSH} and P_{prec} (Table 1), but no peaks at the P_{orb} by Pretorius & Knigge. However, there are two other visible peaks at $0^{\text{d}}.07885(14)$ and $0^{\text{d}}.07639(13)$, which correspond to $P_{\text{orb}}/2$ by Pretorius & Knigge and $P_{\text{nSH}}/2$ respectively.

4 DISCUSSION

4.1 Mass-ratio estimates

By using smoothed particle hydrodynamic (SPH) simulations of tilted accretion discs, Wood et al. (2009) found that the relation between the mass ratio and the nSH deficit is well-represented by

$$q(\varepsilon_-) = -0.192|\varepsilon_-|^{0.5} + 10.37|\varepsilon_-| - 99.83|\varepsilon_-|^{1.5} + 451.1|\varepsilon_-|^2. \quad (3)$$

This result has been supported by other works using related SPH simulations (Montgomery 2009a; Thomas & Wood 2015). To compare Equation (3) with observations, we searched for NL objects in

⁷ The VSX identifier of this source is USNO-A2.0 0300-28957281.

⁸ ESO Online Digitized Sky Survey: <http://archive.eso.org/dss/dss> (accessed 2022 October).

⁹ https://www.aavso.org/vsx_docs/1544030/3344/USNO-A2.0%200300-28957281.png

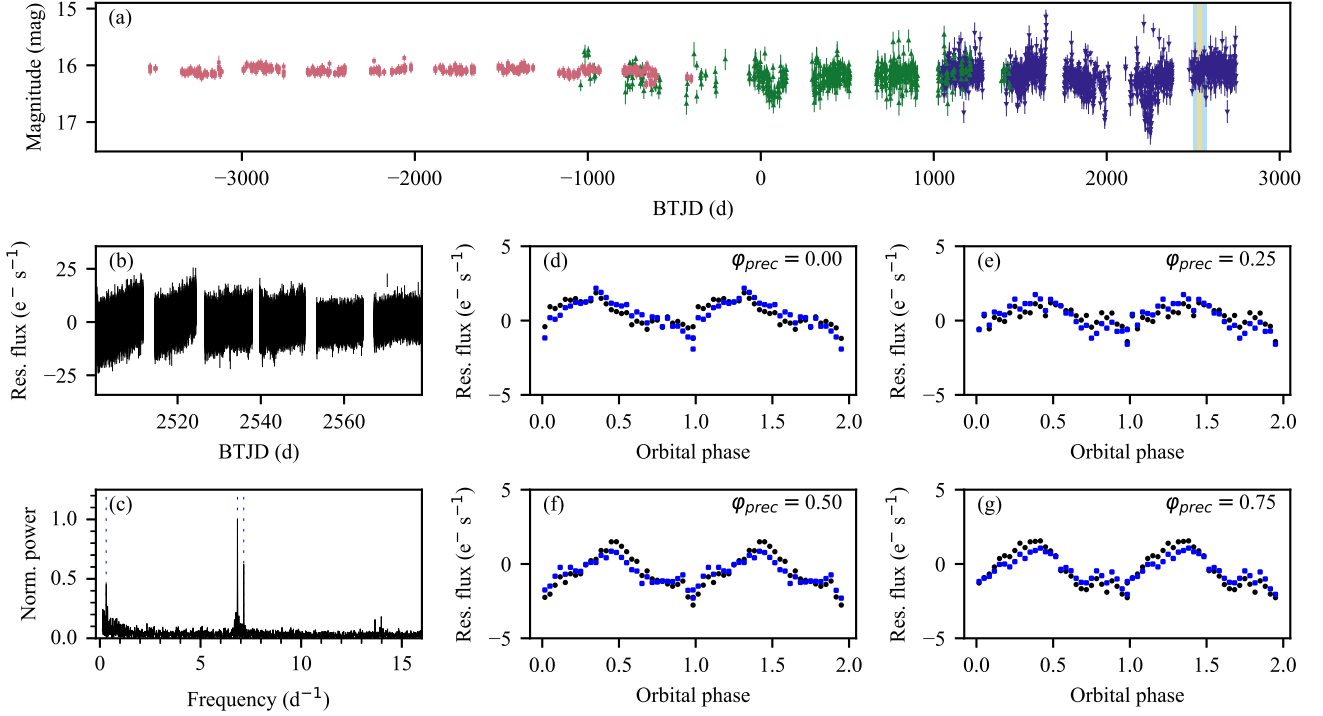


Figure 6. Photometry and analysis of SDSS-090113. (a) Long-term photometry from: ASAS-SN *g* (purple downward triangles), ASAS-SN *V* (green upward triangles), Catalina *V* (pink squares). Temporal coverage of TESS: Sector 44 (light blue), Sector 45 (yellow), Sector 46 (light blue). (b) Residual (mean-subtracted) SAP flux from TESS data. (c) Associated LS periodogram of (b), with indications of P_{prec} , P_{orb} , P_{nSH} signals from Table 1 (blue dashes). Data from (b) was smoothed by a fourth-order Savitzky-Golay filter of window size 10 d before constructing the periodogram. This was done solely for the sake of clear identification of P_{prec} by the reader, and not for periodicity measurements. (d)–(g) Binned orbital profiles around disc precession phases $\varphi_{\text{prec}} = 0.00, 0.25, 0.50, 0.75$ with nSH subtraction (blue squares) and without one (black circles). The typical standard deviation of data in bins is $4 \text{ e}^- \text{ s}^{-1}$. SDSS-090113 appears to have shallow grazing eclipses that are barely detectable for some φ_{prec} . Observed eclipses vary in depth and width for different φ_{prec} . This could be explained by a secondary that partially covers the tilted disc only when the projected area of the disc is large.

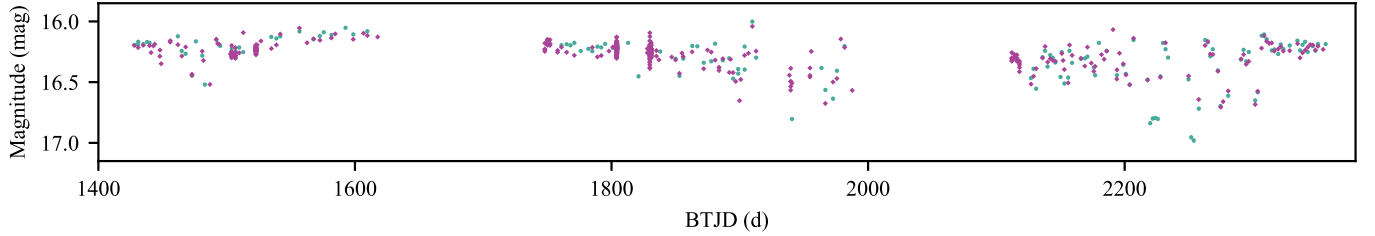


Figure 7. IW And episodes of SDSS-090113 in ZTF *g* (teal circles) and ZTF *r* (magenta diamonds). Three seasons of photometry are shown. The first season starts with oscillations that are terminated by brightening. This is one of the defining features of the IW And phenomenon (Kato 2019; Kato et al. 2022). The second season shows the beginning of a new oscillatory episode that is variable in amplitude. The episode continues in the third season and abruptly ends at BTJD 2315.

literature for which superhump deficits and mass ratios were measured independently from one another. Our reasoning is that NLs share three main similarities with our discovered CVs: (1) their P_{orb} are of the same order, (2) they have steady, hot and luminous discs, (3) samples of both populations exhibit VY-Scl behaviour. Using the sample of NLs with nSH signatures, given in Bruch (2023), we were able to find twelve such objects, which we list in Table 2. Figure 10(a) compares their measurements with the $q(\varepsilon_-)$ relations provided by Montgomery (2009a) and Wood et al. (2009). We share the concern that both works underestimate $q(\varepsilon_-)$ with respect to past measurements in literature.

There exists a different approach that could estimate mass ratios using nSHs. By making some assumptions, a $q(\varepsilon_-)$ relation can be derived in the following manner. Through linear perturbation theory, Papaloizou & Terquem (1995) derived the precession rate ω_{prec} of a differentially rotating fluid disc with a mass profile $\Sigma(r)$:

$$\omega_{\text{prec}} = -\frac{3}{4} \frac{GM_2}{a^3} \frac{\int \Sigma r^3 dr}{\int \Sigma \Omega r^3 dr} \cos \theta, \quad (4)$$

where a is the orbital separation, $\Omega(r) = \sqrt{GM_1/r^3}$ is the Keplerian angular velocity profile of the disc, and θ is the disc tilt with respect to the orbital plane. For a power-law mass profile $\Sigma(r) \propto r^n$, Osaki

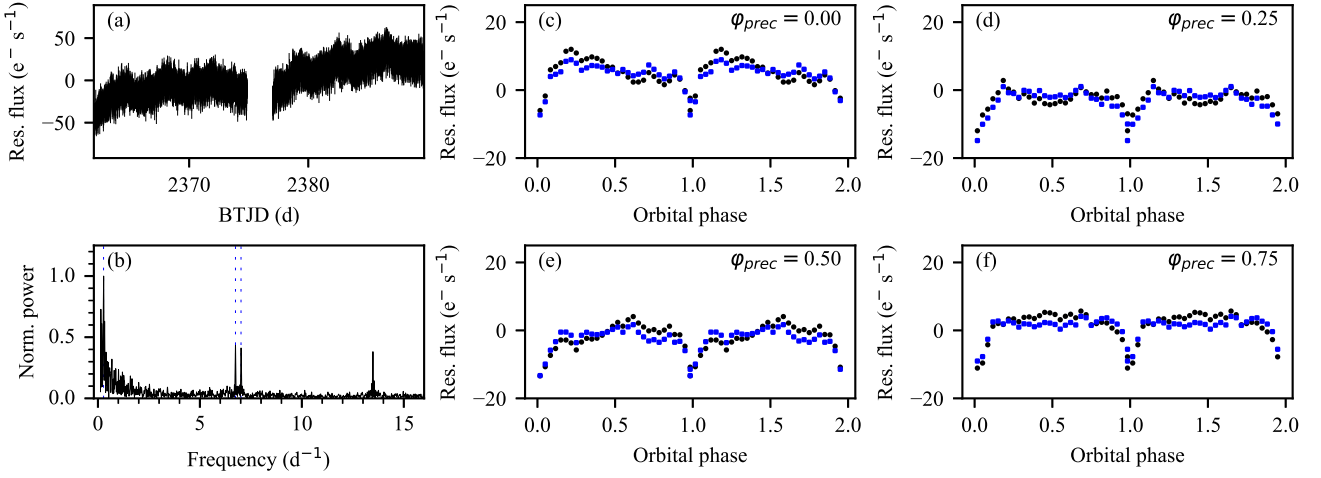


Figure 8. Photometry and analysis of Gaia-593107. (a) Residual (mean-subtracted) SAP flux from TESS data. (b) Associated LS periodogram of (a), with indications of P_{prec} , P_{orb} , P_{nSH} signals from Table 1 (blue dashes). (c)–(f) Binned orbital profiles around disc precession phases $\varphi_{\text{prec}} = 0.00, 0.25, 0.50, 0.75$ with nSH subtraction (blue squares) and without one (black circles). The typical standard deviation of data in bins is $8 \text{ e}^- \text{ s}^{-1}$. Similar to the other eclipsing binaries in our sample, the secondary is expected to be the most irradiated in panels (c) and (e), where the observed out-of-eclipse profile is non-flat. In panels (d) and (f), these profiles are mostly flat, and the system brightness does not seem to increase near $\varphi_{\text{orb}} = 0.5$.

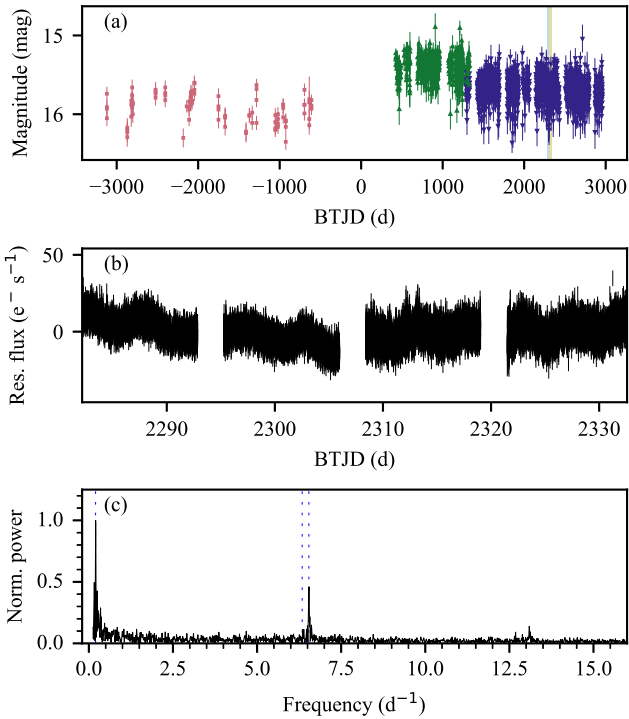


Figure 9. Photometry and analysis of PK-103959. (a) Long-term photometry from: ASAS-SN *g* (purple downward triangles), ASAS-SN *V* (green upward triangles), Catalina *V* (pink squares). Temporal coverage of TESS: Sector 36 (light blue), Sector 37 (yellow). (b) Residual (mean-subtracted) SAP flux from TESS data. (c) Associated LS periodogram of (b), with indications of P_{prec} , P_{orb} , P_{nSH} signals from Table 1 (blue dashes).

& Kato (2013) derived that

$$\frac{\nu_{\text{prec}}}{\nu_{\text{orb}}} = -\frac{3}{4} \frac{2.5+n}{4+n} \frac{q}{\sqrt{1+q}} \left(\frac{R_d}{a} \right)^{1.5} \cos \theta, \quad (5)$$

where $\nu = \omega/2\pi$ and R_d is the disc radius.¹⁰ Using Equations (1), (2) and a mass profile of a steady-state disc given by $n = -0.75$ (Shakura & Sunyaev 1973), Equation (5) can be reduced to

$$\frac{\varepsilon_-}{1+\varepsilon_-} = -\frac{21}{52} \frac{q}{\sqrt{1+q}} \left(\frac{R_d}{a} \right)^{1.5} \cos \theta. \quad (6)$$

A similar derivation can be found in Montgomery (2009b). This shows that ε_- depends on three parameters: the mass ratio q , the disc tilt θ and the fractional disc radius R_d/a . The third can be reasoned to be a function of q as follows. Suppose that in our systems with discovered nSHs, accretion discs are in steady state most of the time. Then, R_d approaches the tidal truncation radius r_{tidal} . Paczynski (1977, Table 1) provided a functional dependence $r_{\text{tidal}}(q)$. Later, Warner (1995) proposed the approximation

$$r_{\text{tidal}} = \frac{0.60a}{1+q} \quad (7)$$

for $0.03 < q < 1$. This is a good approximation in all regions but near $q = 0.7$, where $r_{\text{tidal}}(q)$ is underestimated. Using it would reduce Equation (6) to

$$\frac{\varepsilon_-}{1+\varepsilon_-} = -\frac{0.188q}{(1+q)^2} \cos \theta, \quad (8)$$

which does not describe well observational data for $q > 0.4$ (see dotted line in Figure 10(b)). Because of this, we do not use Equation (8). Instead, we linearly interpolate between data given in Paczynski (1977, Table 1) in order to evaluate R_d/a in Equation (6).

The other independent variable in Equation (6) is the disc tilt θ . Smak (2009) predicts that disc tilts should not exceed $\theta_{\text{max}} = 7^\circ$ for CVs. In their photometric analysis of KIC 9406652, Kimura et al. (2020b) concluded that θ varies between 0 – 3° over the course of 1500 days. Such range of θ allows the assumption $\cos \theta \simeq 1$, which is accurate to within one per cent. This motivates us to compute a $q(\varepsilon_-)$ curve for $\cos \theta = 1$ and compare it against measurements of Table 2 objects (Figure 10(b); Table A2). The $q(\varepsilon_-)$ relation becomes two-fold degenerate in q from about $|\varepsilon_-| > 0.048$.

¹⁰ We note that precession is retrograde, which implies $\omega_{\text{prec}}, \nu_{\text{prec}} < 0$.

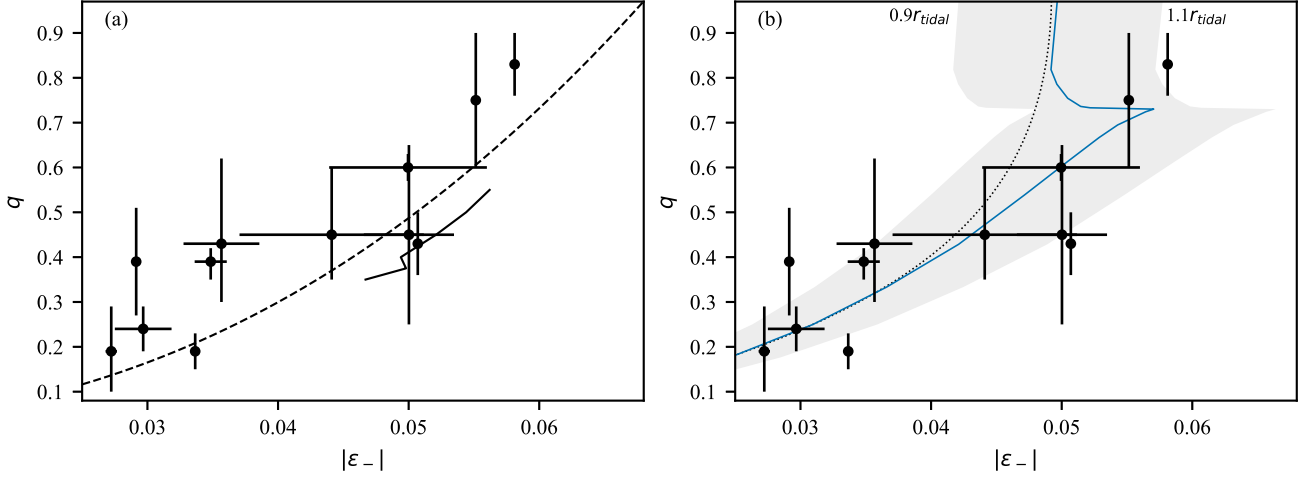


Figure 10. Different $q(\varepsilon_-)$ relations against NL variables with ε_- , q measurements from Table 2. (a) Solid line: [Montgomery \(2009a\)](#), Dashed line: [Wood et al. \(2009\)](#). Both relations underestimate $q(\varepsilon_-)$ for given measurements. (b) Dotted line: Equation (8), derived from the approximation by [Warner \(1995\)](#) used in Equation (6). This fails to accurately describe [Paczynski \(1977\)](#) in q regimes near 0.7. Blue curve: a computed $q(\varepsilon_-)$ relation from our treatment in Section 4.1 that makes use of [Paczynski \(1977\)](#). Shaded region: solutions between $R_d = 0.9-1.1r_{\text{tidal}}$. All measurements belong to this region within uncertainty.

Table 2. A list of NLs with independently measured superhump deficit ε_- and mass ratio q . Equatorial coordinates come from Gaia DR3 and are in the J2000 epoch. Other references: (a) [Gies et al. \(2013\)](#); (b) [Africano et al. \(1978\)](#); (c) [Smak \(2019\)](#); (d) [Subebekova et al. \(2020\)](#); (e) [Skillman et al. \(1995\)](#); (f) [Bruch et al. \(2022\)](#); (g) [Rodríguez-Gil et al. \(2020\)](#); (h) [Kozhevnikov \(2007\)](#); (i) [Araujo-Betancor et al. \(2003\)](#); (j) [Boyd et al. \(2017\)](#); (k) [Wu et al. \(2002\)](#); (l) [Huber et al. \(1998\)](#); (m) [Taylor et al. \(1998\)](#); (n) [Hoard & Szkody \(1997\)](#); (o) [Patterson \(1999\)](#); (p) [Arenas et al. \(2000\)](#); (q) [Peters & Thorstensen \(2006\)](#); (r) [Patterson et al. \(1997\)](#); (s) [Neustroev et al. \(2011\)](#); (t) [de Miguel et al. \(2016\)](#); (u) [Szkody & Howell \(1993\)](#); (v) [Bruch \(2023\)](#); (w) [Gülseçen et al. \(2009\)](#); (x) [Hellier \(1993\)](#); (y) [Bruch \(2022\)](#).

Name	RA	Dec	q	P_{orb}	P_{nSH}	$ \varepsilon_- $
KIC 9406652	19 ^h 31 ^m 29 ^s .15	+45°59′06″.1	$^{a}0.83 \pm 0.07$	$^{a}0.25450(2)$	$^{a}0.23971(2)$	0.0581(1)
RW Tri	02 ^h 25 ^m 36 ^s .16	+28°05′50″.9	$^{d}0.60 \pm 0.03$	$^{b}0.23188324(4)$	$^{c}0.2203(14)$	0.050(6)
MV Lyr	19 ^h 07 ^m 16 ^s .29	+44°01′07″.9	$^{e}0.43^{+0.19}_{-0.13}$	$^{e}0.1329(4)$	$^{f}0.12816(1)$	0.036(3)
KR Aur	06 ^h 15 ^m 43 ^s .92	+28°35′08″.6	$^{g}0.39^{+0.03}_{-0.04}$	$^{g}0.16277164(5)$	$^{h}0.1571(2)$	0.035(1)
DW UMa	10 ^h 33 ^m 52 ^s .88	+58°46′54″.7	$^{i}0.39 \pm 0.12$	$^{i}0.136606499(3)$	$^{j}0.132626(9)$	0.02914(7)
TT Ari	02 ^h 06 ^m 53 ^s .08	+15°17′41″.9	$^{k}0.19 \pm 0.04$	$^{k}0.1375504(17)$	$^{f}0.132921(2)$	0.03366(2)
V592 Cas	00 ^h 20 ^m 52 ^s .22	+55°42′16″.2	$^{l}0.19^{+0.10}_{-0.09}$	$^{m}0.115063(1)$	$^{m}0.11193(5)$	0.0272(4)
BH Lyn	08 ^h 22 ^m 36 ^s .05	+51°05′24″.6	$^{n}0.45^{+0.15}_{-0.10}$	$^{n}0.15587520(5)$	$^{o}0.1490(11)$	0.044(7)
V603 Aql	18 ^h 48 ^m 54 ^s .64	+00°35′02″.9	$^{p}0.24 \pm 0.05$	$^{q}0.13820103(8)$	$^{r}0.1341(3)$	0.030(2)
UX UMa	13 ^h 36 ^m 40 ^s .95	+51°54′49″.4	$^{s}0.43 \pm 0.07$	$^{t}0.19667118(19)$	$^{t}0.186700(11)$	0.05070(6)
AY Psc	01 ^h 36 ^m 55 ^s .46	+07°16′29″.3	$^{u}0.45 \pm 0.2$	$^{v}0.217320654(4)$	$^{w}0.20645(75)$	0.050(3)
TV Col	05 ^h 29 ^m 25 ^s .53	−32°49′03″.9	$^{x}0.75 \pm 0.15$	$^{y}0.22860010(2)$	$^{y}0.215995(1)$	0.055140(4)

There are several systems that lie far from our computed curve. However, they would all agree with a $q(\varepsilon_-)$ relation where R_d is between $0.9-1.1r_{\text{tidal}}$ (also in Figure 10(b)). It becomes apparent that the curve is much more sensitive to changes in R_d than to changes in θ . On this basis, we compute three curves for different $R_d = 0.9r_{\text{tidal}}, 1.0r_{\text{tidal}}, 1.1r_{\text{tidal}}$ and then we graphically solve q for our measured ε_- . Our mass-ratio estimates are listed in Table 3.

Systems with smaller $|\varepsilon_-|$ tend to be better constrained in q . For example, PK-103959 has the lowest $|\varepsilon_-| = 0.0308(22)$ in our sample, and its mass ratio shows little variation for different values of R_d . Conversely, SDSS-090113 has the largest measured $|\varepsilon_-|$ in our sample. For different R_d , its q estimates differ significantly with respect to statistical uncertainty.

Table 3. Estimates of the mass ratio q of Table 1 systems for disc radii $R_d = 0.9r_{\text{tidal}}, 1.0r_{\text{tidal}}, 1.1r_{\text{tidal}}$ from [Paczynski \(1977\)](#), using the methods described in Section 4.1. Upper bounds of q entering the region of two-fold degeneracy are labeled with an asterisk.

Name	$q(\varepsilon_-)$		
	$0.9r_{\text{tidal}}$	$1.0r_{\text{tidal}}$	$1.1r_{\text{tidal}}$
HBHA 4204-09	$0.38^{+0.05}_{-0.05}$	$0.28^{+0.03}_{-0.03}$	$0.22^{+0.02}_{-0.02}$
Gaia-468436	$0.60^{+0.09*}_{-0.13}$	$0.43^{+0.10}_{-0.08}$	$0.33^{+0.07}_{-0.06}$
KQ Mon	$0.59^{+0.11*}_{-0.11}$	$0.42^{+0.09}_{-0.07}$	$0.32^{+0.06}_{-0.05}$
SDSS-090113	$0.64^{+0.04*}_{-0.04}$	$0.46^{+0.03}_{-0.03}$	$0.35^{+0.02}_{-0.02}$
Gaia-593107	$0.52^{+0.11}_{-0.10}$	$0.38^{+0.08}_{-0.07}$	$0.29^{+0.06}_{-0.05}$
PK-103959	$0.33^{+0.04}_{-0.04}$	$0.25^{+0.03}_{-0.03}$	$0.20^{+0.02}_{-0.02}$

4.2 Orbital inclination estimates

The eclipse width at half depth $\Delta\varphi_{\text{orb}}$ is a reasonable measure of the primary-eclipse duration in the assumption of an axisymmetric disc (Warner 1995, Section 2.6.2). This duration can be used to determine the orbital inclination i by the relationship

$$\sin^2 i \approx \frac{1 - R_L(2)^2}{\cos^2(2\pi\varphi_p)}, \quad (9)$$

where $R_L(2)$ is the radius of the secondary star, and $\pm\varphi_p$ are the phases of mid-immersion and mid-emergence of the primary star (Horne 1985; Warner 1995).¹¹ The Roche-lobe radius approximation by Eggleton (1983)

$$R_L(2) = \frac{0.49q^{2/3}}{0.6q^{2/3} + \ln(1 + q^{1/3})} \quad (10)$$

can be used to substitute $R_L(2)$ in Equation (9), such that the relation can retrieve i using only $\Delta\varphi_{\text{orb}}$ and the superhump-derived q . We use this relation to constrain i for HBHA 4204-09, SDSS-090113 and Gaia-593107, which are eclipsing systems. We measured $\Delta\varphi_{\text{orb}}$ on nSH-subtracted data.

HBHA 4204-09 has a deep eclipse, with $\Delta\varphi_{\text{orb}} = 0.049(4)$. Using our value of $q \approx 0.29(3)$, we compute $i = 77(1)^\circ$. On the other hand, SDSS-090113 shows grazing eclipses of variable depth and width that disappear completely for some φ_{prec} . For this reason, we can assume $\Delta\varphi_{\text{orb}} \approx 0$. With our value of $q \approx 0.47(4)$, we compute $i = 71.6(4)^\circ$. For the last eclipsing system in our sample, Gaia-593107, we measure $\Delta\varphi_{\text{orb}} = 0.06(2)$. This eclipse width, combined with $q \approx 0.38(8)$, gives an orbital inclination $i = 76(3)^\circ$.

5 CONCLUSIONS

In this work we present results from a search for nSHs in poorly studied CVs. We initially cross-matched TESS light-curve data with the VSX catalogue for objects labelled as CV or NL. We manually inspected LS periodograms of objects from this query ($n = 180$), and then selected targets with at least two neighbouring periodicities above the period gap, including one large-period signal that matches the beating of the former two. This resulted in six systems with nSHs, which we list in Table 1.

Spectroscopic measurements of P_{orb} were available for only one of the six aforementioned systems. For the rest, we used a couple of methods to recognise P_{orb} signatures in their LS periodograms. Three systems had their orbital period determined by the presence of eclipses. For the last two, P_{orb} was identified using the φ_{prec} -dependent irradiation of the secondary caused by the precessing tilted disc (see Section 2.2). For all systems, the light maximum in the orbital phase profile was found to shift to earlier φ_{orb} , as φ_{prec} advances. This is strong evidence of nSHs (Kimura et al. 2020b; Kimura & Osaki 2021) and supports our findings. For SDSS-090113, a peculiar behaviour was observed in ZTF photometry (Figure 7), which is similar to what is observed in IW And stars (Kato 2019). For Gaia-46843, two Z Cam-like episodes in ASAS-SN data were found, which take place after drops in brightness of about 0.5 mag (Figure 4).

Determined periodicities from TESS photometry can constrain some physical parameters of CV systems. The dependence between the nSH deficit ε_- and the system mass ratio q has been explored in several works already (e.g. Wood et al. 2009; Montgomery 2009a).

Referenced $q(\varepsilon_-)$ relations, however, underestimate independent measurements of q and ε_- , which gives some ground for concern (Figure 10(a)). We tried to come to a better $q(\varepsilon_-)$ relation by using the precession rate of a differentially rotating steady-state disc that extends to the maximum tidal truncation radius r_{tidal} . This, in combination with the $r_{\text{tidal}}(q)$ relation given in Paczynski (1977, Table 1), resulted in better agreement with independent observations (Figure 10(b)). Mass-ratio estimates using this method are given in Table 3 for different disk radii $R_d = 0.9r_{\text{tidal}}, 1.0r_{\text{tidal}}, 1.1r_{\text{tidal}}$. For the three systems that are eclipsing, we used the eclipse-mapping techniques described by Horne (1985); Warner (1995) to compute the orbital inclination i with our values of q .

There are several subtle points that bear discussion. SAP light curves from TESS-SPOC may contain instrumental effects that could affect LS periodogram measurements; and photometry itself may be contaminated by nearby sources. To address the former, we repeated our methods on PDCSAP data, and found small differences in comparison to Table 1 measurements. Regarding the latter, we used mean-subtracted fluxes in all analysis, which mitigates effects by non-variable contaminating objects. None of our systems have bright sources in their vicinity, except the case of Gaia-593107, which is discussed in Section 3.5.

Our variant of the nSH subtraction method in Kimura & Osaki (2021) shares the same shortcomings. If the nSH profile is time-dependent, it cannot be fully subtracted. In addition, the mass-transfer stream could happen to obstruct some parts of the disc, causing the light maximum to occur at earlier orbital phases φ_{orb} (Kimura et al. 2020b). Inhomogeneities in the stellar surface brightness of the secondary can produce similar effects, shifting the light maximum to earlier or to later φ_{orb} .

The technique of using irradiation of the secondary in order to determine P_{orb} is entirely based on photometry, and spectroscopic measurements of P_{orb} could support its feasibility. In addition, radial-velocity analysis would put constraints on mass ratios, and would test the $q(\varepsilon_-)$ relation we consider in Section 4.1. The newly discovered systems in this work are therefore strongly encouraged for follow-up spectroscopic observations.

ACKNOWLEDGEMENTS

This work includes data collected by the TESS mission and made use of LIGHTKURVE, a Python package for Kepler and TESS data analysis (Lightcurve Collaboration et al. 2018). Funding for the TESS mission is provided by the NASA's Science Mission Directorate. This work has made use of the NASA/IPAC Infrared Science Archive, which is funded by the National Aeronautics and Space Administration and operated by the California Institute of Technology.

The CSS survey is funded by the National Aeronautics and Space Administration under Grant No. NNG05GF22G issued through the Science Mission Directorate Near-Earth Objects Observations Program. The CRTS survey is supported by the U.S. National Science Foundation under grants AST-0909182 and AST-1313422.

We used the following Python packages for data analysis and visualisation: NUMPY (Harris et al. 2020), SCIPY (Virtanen et al. 2020), PANDAS (McKinney 2010; The Pandas Development Team 2022), MATPLOTLIB (Hunter 2007) and UNCERTAINTIES (Lebigot 2010).

We are grateful to R. K. Zamanov and to A. A. Kurtenkov for their advice during the preparation of this work. We thank the anonymous referee for their time and their effort. We acknowledge the grants KPI-06-H28/2 and KPI-06-M58/2 from the Bulgarian National Science Fund. Both authors contributed equally to this work. It is appre-

¹¹ From here, $\varphi_p \equiv \Delta\varphi_{\text{orb}}/2$.

ciated that our last names considerably simplified the issue of author ordering.

DATA AVAILABILITY

This work contains publicly available data from the sky surveys TESS, ASAS-SN, CSS, CRTS, and ZTF, all of which can be found in their corresponding databases.

REFERENCES

- Africano J. L., Nather R. E., Patterson J., Robinson E. L., Warner B., 1978, *PASP*, **90**, 568
- Araujo-Betancor S., et al., 2003, *ApJ*, **583**, 437
- Arenas J., Catalán M. S., Augustejn T., Retter A., 2000, *MNRAS*, **311**, 135
- Bajer M., 2019, VSX Discovery of BMAM-V424, <https://www.aavso.org/vsx/index.php?view=detail.top&oid=1260092>
- Bellm E. C., et al., 2019, *PASP*, **131**, 018002
- Bond H. E., 1979, in van Horn H. M., Weidemann V., Savedoff M. P., eds, IAU Colloq. 53: White Dwarfs and Variable Degenerate Stars. p. 495
- Boyd D. R. S., et al., 2017, *MNRAS*, **466**, 3417
- Bruch A., 2022, *MNRAS*, **514**, 4718
- Bruch A., 2023, *MNRAS*, **519**, 352
- Drake A. J., et al., 2009, *The Astrophysical Journal*, **696**, 870
- Eggleton P. P., 1983, *ApJ*, **268**, 368
- Förster F., et al., 2021, *AJ*, **161**, 242
- Gies D. R., et al., 2013, *ApJ*, **775**, 64
- Gülsecen H., Retter A., Liu A., Esenoğlu H., 2009, *New Astron.*, **14**, 330
- Harris C. R., et al., 2020, *Nature*, **585**, 357
- Hellier C., 1993, *MNRAS*, **264**, 132
- Hellier C., 2001, *Cataclysmic Variable Stars*. Springer
- Hirose M., Osaki Y., 1990, *PASJ*, **42**, 135
- Hoard D. W., Szkody P., 1997, *ApJ*, **481**, 433
- Horne K., 1985, *MNRAS*, **213**, 129
- Howell S. B., 2004, in Vriellmann S., Cropper M., eds, *Astronomical Society of the Pacific Conference Series Vol. 315, IAU Colloq. 190: Magnetic Cataclysmic Variables*. p. 353 ([arXiv:astro-ph/0302368](https://arxiv.org/abs/astro-ph/0302368))
- Huber M. E., Howell S. B., Ciardi D. R., Fried R., 1998, *PASP*, **110**, 784
- Hunter J. D., 2007, *Computing in Science & Engineering*, **9**, 90
- Jayasinghe T., et al., 2018, *MNRAS*, **477**, 3145
- Jenkins J. M., et al., 2016, in Chiozzi G., Guzman J. C., eds, *Society of Photo-Optical Instrumentation Engineers (SPIE) Conference Series Vol. 9913, Software and Cyberinfrastructure for Astronomy IV*. p. 99133E, [doi:10.1117/12.2233418](https://doi.org/10.1117/12.2233418)
- Kato T., 2019, *PASJ*, **71**, 20
- Kato T., 2022, arXiv e-prints, [p. arXiv:2205.00632](https://arxiv.org/abs/2205.00632)
- Kato T., et al., 2009, *PASJ*, **61**, S395
- Kato T., et al., 2017, *PASJ*, **69**, 75
- Kato T., et al., 2022, arXiv e-prints, [p. arXiv:2202.11832](https://arxiv.org/abs/2202.11832)
- Kimura M., Osaki Y., 2021, *PASJ*, **73**, 1225
- Kimura M., Osaki Y., Kato T., Mineshige S., 2020a, *PASJ*, **72**, 22
- Kimura M., Osaki Y., Kato T., 2020b, *PASJ*, **72**, 94
- Kinemuchi K., Barclay T., Fanelli M., Pepper J., Still M., Howell S. B., 2012, *PASP*, **124**, 963
- King A. R., Cannizzo J. K., 1998, *ApJ*, **499**, 348
- Kochanek C. S., et al., 2017, *PASP*, **129**, 104502
- Kohoutek L., Wehmeyer R., 1999, *A&AS*, **134**, 255
- Kozhevnikov V. P., 2007, *MNRAS*, **378**, 955
- Lebigot E. O., 2010, *Uncertainties: A Python Package for Calculations with Uncertainties*
- Lightcurve Collaboration et al., 2018, *Astrophysics Source Code Library*, p. ascl:1812.013
- Livio M., Pringle J. E., 1994, *ApJ*, **427**, 956
- Lomb N. R., 1976, *Ap&SS*, **39**, 447
- Lubow S. H., 1991, *ApJ*, **381**, 259
- McKinney W., 2010, in *Python in Science Conference*. Austin, Texas, pp 56–61, [doi:10.25080/Majora-92bf1922-00a](https://doi.org/10.25080/Majora-92bf1922-00a)
- Montgomery M. M., 2009a, *MNRAS*, **394**, 1897
- Montgomery M. M., 2009b, *ApJ*, **705**, 603
- Mösenlechner G., Paunzen E., Pelisoli I., Seelig J., Stidl S., Maitzen H. M., 2022, *A&A*, **657**, A27
- Neustroev V. V., Suleimanov V. F., Borisov N. V., Belyakov K. V., Shearer A., 2011, *MNRAS*, **410**, 963
- Osaki Y., Kato T., 2013, *PASJ*, **65**, 95
- Paczynski B., 1977, *ApJ*, **216**, 822
- Papaloizou J. C. B., Terquem C., 1995, *MNRAS*, **274**, 987
- Parker Q. A., et al., 2005, *MNRAS*, **362**, 689
- Patterson J., 1999, in Mineshige S., Wheeler J. C., eds, *Disk Instabilities in Close Binary Systems*. p. 61
- Patterson J., Kemp J., Saad J., Skillman D. R., Harvey D., Fried R., Thorstensen J. R., Ashley R., 1997, *PASP*, **109**, 468
- Peters C. S., Thorstensen J. R., 2006, *PASP*, **118**, 687
- Prestgard T., 2020, VSX Discovery of USNO-A2.0 0300-28957281, <https://www.aavso.org/vsx/index.php?view=detail.top&oid=1544030>
- Pretorius M. L., Knigge C., 2008, *MNRAS*, **385**, 1471
- Raddi R., et al., 2017, *MNRAS*, **472**, 4173
- Ricker G. R., et al., 2015, *Journal of Astronomical Telescopes, Instruments, and Systems*, **1**, 014003
- Rodríguez-Gil P., et al., 2020, *MNRAS*, **494**, 425
- Savitzky A., Golay M. J. E., 1964, *Analytical Chemistry*, **36**, 1627
- Scargle J. D., 1982, *ApJ*, **263**, 835
- Schmidtobreick L., Tappert C., Galli L., Whiting A., 2005, *Information Bulletin on Variable Stars*, **5627**, 1
- Shakura N. I., Sunyaev R. A., 1973, *A&A*, **24**, 337
- Shappee B. J., et al., 2014, *ApJ*, **788**, 48
- Skillman D. R., Patterson J., Thorstensen J. R., 1995, *PASP*, **107**, 545
- Smak J., 2009, *Acta Astron.*, **59**, 419
- Smak J., 2019, *Acta Astron.*, **69**, 79
- Subebekova G., Zharikov S., Tovmassian G., Neustroev V., Wolf M., Hernandez M. S., Kučáková H., Khokhlov S., 2020, *MNRAS*, **497**, 1475
- Szkody P., Howell S. B., 1993, *ApJ*, **403**, 743
- Szkody P., et al., 2009, *AJ*, **137**, 4011
- Taylor C. J., et al., 1998, *PASP*, **110**, 1148
- The Pandas Development Team 2022, *Pandas-Dev/Pandas: Pandas*, Zenodo, [doi:10.5281/ZENODO.3509134](https://doi.org/10.5281/ZENODO.3509134)
- Thomas D. M., Wood M. A., 2015, *ApJ*, **803**, 55
- Virtanen P., et al., 2020, *Nature Methods*, **17**, 261
- Warner B., 1995, *Cataclysmic Variable Stars*. Cambridge Astrophysics, Cambridge University Press, [doi:10.1017/CBO9780511586491](https://doi.org/10.1017/CBO9780511586491)
- Watson C. L., Henden A. A., Price A., 2006, *Society for Astronomical Sciences Annual Symposium*, **25**, 47
- Whitehurst R., 1988, *MNRAS*, **232**, 35
- Wolfe A., Sion E. M., Bond H. E., 2013, *AJ*, **145**, 168
- Wood M. A., Thomas D. M., Simpson J. C., 2009, *MNRAS*, **398**, 2110
- Wu X., Li Z., Ding Y., Zhang Z., Li Z., 2002, *ApJ*, **569**, 418
- Zacharias N., Monet D. G., Levine S. E., Urban S. E., Gaume R., Wycoff G. L., 2004, in *American Astronomical Society Meeting Abstracts*. p. 48.15
- de Miguel E., et al., 2016, *MNRAS*, **457**, 1447

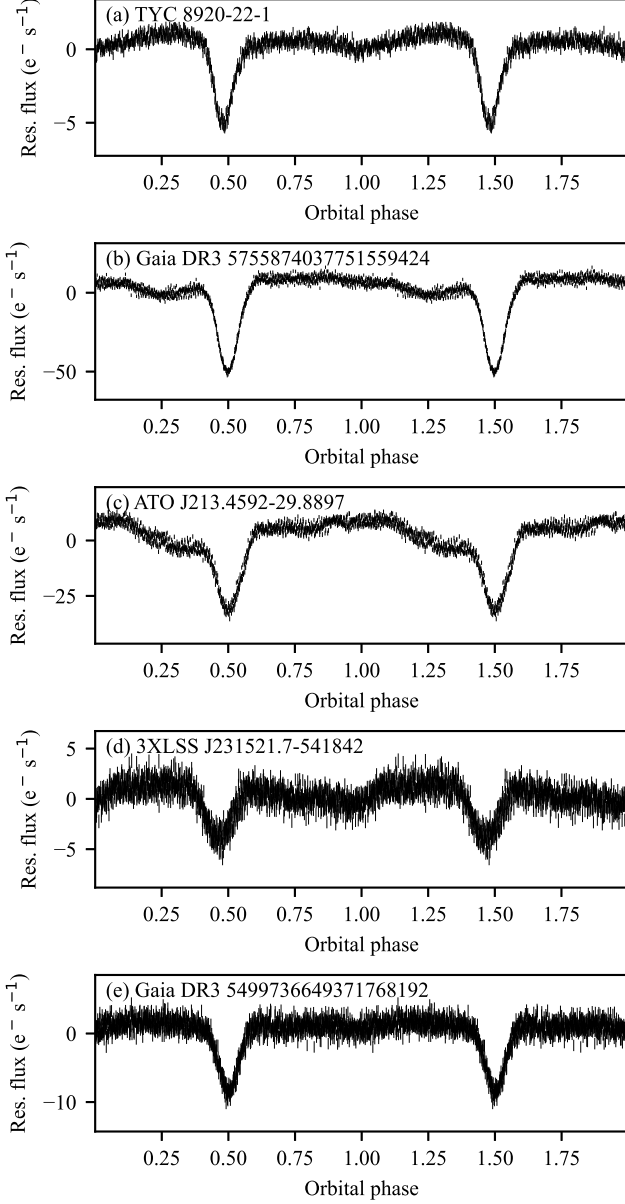
APPENDIX A: EXTRA MATERIAL

This appendix contains orbital phase curves (Figure A1) and a list of P_{orb} measurements (Table A3) of discovered eclipsing binaries with no nSH behaviour. Our calculated $q(\varepsilon_-)$ curves using the tidal truncation disc radii relation $r_{\text{tidal}}(q)$ in Paczynski (1977) are shown in Table A2. Computed values can be approximated by

$$|\varepsilon_-| = \frac{aq}{(1+q)^b}, \quad (\text{A1})$$

Table A1. Equation (A1) fit coefficients a and b that approximate Table A2 data for different values of R_d .

R_d	a	b	$ \varepsilon_- $ interval
$0.9r_{\text{tidal}}$	0.155	1.706	[0.006, 0.041]
$1.0r_{\text{tidal}}$	0.182	1.694	[0.006, 0.048]
$1.1r_{\text{tidal}}$	0.210	1.680	[0.006, 0.057]

**Figure A1.** Orbital phase curves of Table A3 systems. Light curves were smoothed by a fourth-order Savitzky-Golay filter of window size 10 d before folding. Orbital phases are offset with +0.50 for the sake of clarity.

where a and b are fit coefficients. Values of best fits are given in Table A1 for $R_d = 0.9r_{\text{tidal}}, 1.0r_{\text{tidal}}, 1.1r_{\text{tidal}}$.

This paper has been typeset from a \LaTeX file prepared by the author.

Table A2. Tabular form of our derived $q(\varepsilon_-)$ relation for $R_d = 0.9 - 1.1r_{\text{tidal}}$ using r_{tidal} from Paczynski (1977, Table 1).

$ \varepsilon_- $	$q(\varepsilon_-)$		
	$0.9r_{\text{tidal}}$	$1.0r_{\text{tidal}}$	$1.1r_{\text{tidal}}$
0.006	0.039	0.032	0.031
0.007	0.046	0.038	0.033
0.008	0.053	0.044	0.038
0.009	0.061	0.05	0.043
0.010	0.069	0.057	0.048
0.011	0.077	0.064	0.054
0.012	0.086	0.071	0.060
0.013	0.095	0.078	0.066
0.014	0.104	0.085	0.071
0.015	0.113	0.093	0.078
0.016	0.124	0.101	0.084
0.017	0.135	0.108	0.091
0.018	0.145	0.117	0.097
0.019	0.156	0.126	0.104
0.020	0.167	0.135	0.110
0.021	0.178	0.144	0.118
0.022	0.191	0.153	0.126
0.023	0.205	0.162	0.134
0.024	0.218	0.171	0.142
0.025	0.232	0.181	0.149
0.026	0.246	0.193	0.157
0.027	0.262	0.204	0.165
0.028	0.279	0.216	0.173
0.029	0.297	0.227	0.182
0.030	0.314	0.239	0.192
0.031	0.332	0.251	0.201
0.032	0.352	0.265	0.211
0.033	0.373	0.280	0.221
0.034	0.393	0.295	0.231
0.035	0.414	0.310	0.241
0.036	0.436	0.324	0.251
0.037	0.461	0.340	0.264
0.038	0.487	0.358	0.277
0.039	0.513	0.375	0.289
0.040	0.539	0.392	0.302
0.041	0.566	0.410	0.315
0.042		0.427	0.328
0.043		0.448	0.341
0.044		0.470	0.356
0.045		0.492	0.371
0.046		0.514	0.386
0.047		0.536	0.401
0.048		0.558	0.415
0.049			0.431
0.050			0.449
0.051			0.468
0.052			0.487
0.053			0.505
0.054			0.524
0.055			0.543
0.056			0.562
0.057			0.581

Table A3. List of discovered eclipsing variables with no superhump signatures. Equatorial coordinates come from Gaia DR3 and are in the J2000 epoch.

Name	RA	Dec	TESS Sector	P _{orb}
TYC 8920-22-1	06 ^h 56 ^m 39 ^s .36	−67°02′16″.8	39	0 ^d .09081(18)
Gaia DR3 5755874037751559424	09 ^h 02 ^m 57 ^s .71	−07°59′19″.9	35	0 ^d .15585(53)
ATO J213.4592-29.8897	14 ^h 13 ^m 50 ^s .22	−29°53′23″.1	38	0 ^d .13879(43)
3XLSS J231521.7-541842	23 ^h 15 ^m 21 ^s .72	−54°18′43″.1	28	0 ^d .14966(54)
Gaia DR3 5499736649371768192	06 ^h 27 ^m 51 ^s .08	−53°45′17″.7	39	0 ^d .15838(53)